ORNL/TM-2015/579
M2FT- 15OR0404024

Preliminary Results on FeCrAl Alloys in the As-received and Welded State Designed to Have Enhanced Weldability and Radiation Tolerance

Kevin G. Field
Maxim N. Gussev
Xunxiang Hu
Yukinori Yamamoto

September 30, 2015

OAK RIDGE NATIONAL LABORATORY
MANAGED BY UT-BATTELLE FOR THE US DEPARTMENT OF ENERGY

ORNL/TM-2015/579
M2FT- 15OR0404024

Nuclear Energy Enabling Technologies (NEET): Reactor Materials

Preliminary Results on FeCrAl Alloys in the As-received and Welded State Designed to Have Enhanced Weldability and Radiation Tolerance

Kevin G. Field, Maxim N. Gussev, Xunxiang Hu, and Yukinori Yamamoto

Date Published: September 30th, 2015

Prepared by
OAK RIDGE NATIONAL LABORATORY
Oak Ridge, Tennessee 37831-6283
managed by
UT-BATTELLE, LLC
for the
US DEPARTMENT OF ENERGY
under contract DE-AC05-00OR22725

CONTENTS

Page

LIST OF FIGURES

Figure **Page**

LIST OF TABLES

Table **Page**

ACKNOWLEDGMENTS

This research was sponsored by the U.S. Department of Energy, Office of Nuclear Energy, for the Nuclear Energy Enabling Technologies (NEET) program for the Reactor Materials effort. This report was authored by UT-Battelle, LLC under Contract No. DE-AC05-00OR22725 with the U.S. Department of Energy. The assistance of Zach Thomas and Jay Ferriday on the thermal aging studies is graciously acknowledged.

1. EXECUTIVE SUMMARY

The present report summarizes and discusses the recent results on developing a modern, nuclear grade FeCrAl alloy designed to have enhanced radiation tolerance and weldability. The alloys used for these investigations are modern FeCrAl alloys based on a Fe-13Cr-5Al-2Mo-0.2Si-0.05Y alloy (in wt.%, designated C35M). Development efforts have focused on assessing the influence of chemistry and microstructure on the fabricability and performance of these newly developed alloys. Specific focus was made to assess the weldability, thermal stability, and radiation tolerance.

Preliminary experimental data on these assessments show promising results for the FeCrAl alloy class within the compositions and microstructures investigated. Results presented in Chapter 6 showed LBW produced sound welds, free of defects and inclusions regardless of the alloy heat investigated. It was found the C35M10TC alloy, an alloy with a 1 wt.% addition of TiC, produced an interesting microstructure in the fusion zone of welds and prohibited excessive grain growth, when compared to the other alloys investigated. It is believed the C35M10TC alloy has a large enough volume fraction of TiC dispersions that do not melt under welding that these inclusions can act as pinning points for grain boundaries promoting less grain growth and hence finer grain structures in the fusion zone of weldments. Future mechanical testing and assessments will determine the impact of this uniquely identified ability for minimal grain growth of the C35M10TC alloy on its performance after welding.

Hydrogen charging, as discussed in Chapter 5, was pursued using two different techniques, gaseous charging and cathodic charging. Due to the low pressures and concentration of hydrogen possible in the gaseous charging system, there was no ability to increase the hydrogen concentration in the C35M alloy above the as-received concentrations. It was determined higher pressures would be needed but this exceeded the limitations of the current configurational test bed and hence was not further pursued. The cathodic charging showed more promising results with preliminary testing producing hydrogen concentrations nearly an order of magnitude higher than the as-received condition for the C35M, C36M, and C37M alloys. Further work seeks to examine how the increased hydrogen concentration in the alloys effects the mechanical properties and relating these observations towards the weldability of the FeCrAl alloy class.

Finally, the thermal stability and phase stability of the candidate FeCrAl alloys was assessed as a precursor to understanding the radiation tolerance of the FeCrAl alloys of interest. Aging at 400°C and 475°C produced results on the phase stability of the alloys, see Chapter 4. It was found that thermal aging resulted in increase hardness in some of the investigated alloys, especially above 100 hrs heat treatment. It is believed this increase in hardness is due to the phase separation of FeCrAl alloys into the Fe-rich α phase and the Cr-rich α' phase. The hardening intensity was found to be Cr composition, Al composition, minor solute addition, time, and temperature dependent. Results indicate a possibility for Mo and Si additions to increase the hardening in the alloys, and hence more investigations are needed to determine the role of minor alloying elements on the phase separation of FeCrAl alloys, particularly with irradiation.

The results presented in the following report indicate the advantages of optimizing both the microstructure and chemistry of FeCrAl alloys to obtain necessary properties and performance for nuclear power production including weldability, thermal stability, and radiation tolerance.

2. INTRODUCTION

Modern FeCrAl alloys with optimized chemistry and microstructure are a promising class of alloys for nuclear power production applications due to their superior oxidation and corrosion resistance in high temperature environments [1, 2]. Additionally, they exhibit other behaviors conducive to reactor core internal applications including having radiation-induced cavity swelling resistance on-par with other ferritic alloy systems [3], high resistance to stress corrosion cracking [4], and maintain mechanical performance at and above typical light water reactor (LWR) conditions [5]. These properties are the driving factors for the current interest of using FeCrAl alloys as a cladding technology with enhanced accident tolerance but could also lend itself to other applications such as a core-internal structural components for fast reactor or advanced reactor designs.

However, fabrication-induced and/or radiation-induced phenomena may limit performance while in service for nuclear power production. Non-nuclear grade FeCrAl alloys are known to be susceptible to cracking during welding, especially in the presence of water vapor or hydrogen [6-9]. The cracking susceptibility has also been shown to be composition dependent with high-Cr and high-Al additions leading to cracking in the fusion zone of a FeCrAl weldment, Figure 1. The ability to successfully weld FeCrAl alloys is key to its application in LWRs. Some success has been made through the use of controlled fusion welding including laser beam welding (LBW) [10] and electron-beam welding, but the studies on the weldability of thin plate and cladding tube at compositions of interest for nuclear applications remains limited. Clearly, a weldable FeCrAl option needs to be explored and the processing parameters optimized.

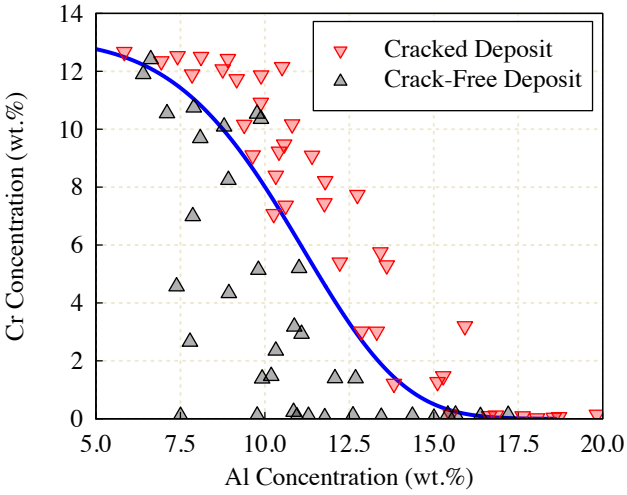

Figure 1: Composition effect on the weldability of FeCrAl alloys after gas tungsten arc welding (GTAW) [9].

Additionally, high-Cr (>8-9 wt.%) FeCrAl alloys with a base ferritic structure are also known to be susceptible to hardening and embrittlement due to the formation of the Cr-rich α' phase under long-term thermal aging [11] which can be accelerated by neutron irradiation [3, 12]. Under neutron irradiation, the formation of other microstructural features including dislocation loops can increase the hardening and embrittlement response of FeCrAl alloys [3]. Preliminary studies on a commercial FeCrAl alloy have shown that microstructural features, such as grain boundaries and dislocation cell networks can alter the radiation response of alloys [13]. The issue is that such microstructural features which could be beneficial towards the radiation tolerance of a FeCrAl weldment can become lost under fusion-based welding leading to fusion zones in weldments with reduced tolerance to radiation. Therefore, the two mechanisms,

fabrication-induced and radiation-induced, can become inter-linked and technologies or strategies must be developed to address these two concerns in parallel.

Preliminary work has begun to address both the weldability and the radiation tolerance of the FeCrAl alloy class in tandem. In particular, two specific mitigation strategies are being developed and evaluated: (1) use of hydrogen trapping sites as a mitigation strategy for susceptibility to cracking during welding and as trapping sites for radiation-induced defects and (2) high-Al content FeCrAl alloys to reduce the precipitation of Cr-rich α' under irradiation.

Work by Dupont et al. [8] has shown that precipitation or secondary phase inclusions in the base FeCrAl structure can act as benign hydrogen trapping sites leading to reduced cracking during welding in the presence of hydrogen. Furthermore, these precipitates could act as trapping sites for point defects under irradiations, similar to the principles of high-sink strength oxide-dispersion strengthened (ODS) steels [14]. Experimental work by Kobayashi and Takasugi [11] and modeling work by Li et al. [15] has indicated that hardening and embrittlement induced by the deleterious Cr-rich α' phase could be mitigated by high-Al additions. Increasing the Al-content leads to a shift in the α – α' phase boundary allowing for higher permissible Cr contents with the possibility for reduced or no α' precipitation either by thermal aging or irradiation. It should be noted that the compositions must be delicately balanced to remain in the regime of weldability detailed by Regina et al. in Figure 1 [9], while still modifying the alloy for reduced α' precipitation.

To investigate the capability of these two mitigation strategies (microstructure and chemistry control), a series of experiments have been conceptualized, performed, and analyzed with a specific focus on understanding the joining and/or radiation response of FeCrAl alloys with the two mitigation strategies intrinsically built into the candidate alloys. The experiments are developed around using, or at a minimum matching, the processing routes used by the nuclear power industry for Fe-based part fabrication, such as warm-rolling/cold-shaping but with single or reduced variable experiments to enable fundamental insights on the weldability and radiation tolerance of candidate FeCrAl alloys. The following report highlights the activities centered on the alloys for investigation with a specific focus on the effects of joining and environmental exposures on the microstructural and mechanical performance of the alloys in the unirradiated state.

3. MATERIALS AND METHODS

3.1 Fabrication of Candidate FeCrAl Alloys

The production and fabrication of candidate FeCrAl alloys have been previously reported on [16, 17]. Details are briefly outlined here for completeness.

Three different types of advanced FeCrAl alloys classes were developed for this study. The three alloy classes are modifications from a base alloy (Fe-13Cr-5Al-2Mo-0.2Si-0.05Y, designated C35M): the first is FeCrAl alloys with Al modifications to increase the possible radiation tolerance of the alloys (designated as C36M and C37M), a FeCrAl alloy with Laves phase dispersions for grain refinement and reduction in hydrogen embrittlement (designated as C35MN), and three FeCrAl alloys with varying amounts of TiC dispersions to act as hydrogen getters (designated as C35M01TC, C35M03TC, and C35M10TC). The selection of these alloys was in order to probe different microstructural and chemical contributions to the weldability and radiation tolerance of FeCrAl alloys. The base C35M alloy was selected as the studies of Field et al. and Yamamoto et al. [3, 5] showed the possibility that a 13 wt.% Cr

variant of FeCrAl with 5 wt.% Al additions could have acceptable radiation tolerance while still maintaining high temperature steam oxidation resistance.

Two processing routes were pursued depending on the alloy heat. The first was vacuum induction melting (VIM), and the other was arc melting with drop casting. VIM produced ingots of ~18 kg, a large volume for continuous research and development efforts while the arc melts produced ingots of ~1 kg for laboratory type investigations. For both processing routes, efforts were taken to control chemistry and hit the nominally specified compositions. Table 1 provides the resulting analyzed compositions and the processing route (VIM or arc melt) for each alloy. It should be noted that based on the cracking map in Figure 1, the alloys of interest lie on the crack – crack-free deposit boundary for GTAW and similar composition have shown cracking when exposed to a hydrogenated environment during GTAW.

Table 1: Candidate FeCrAl alloys processing routes and composition in weight percent.

Alloy	Fe	Cr	Al	Y	Mo	Si	Nb	C	S	O	N	P	Ti
C35M3[1]	79.43	13.06	5.31	0.053	2	0.13	<0.01	0.001	<0.0003	0.0012	0.0003	0.007	<0.01
C36M3[1]	78.8	12.98	6	0.04	1.98	0.18	<0.01	0.003	<0.0003	0.0016	0.0002	<0.002	0.01
C37M[1]	77.49	13.01	7.22	0.081	1.99	0.19	<0.01	0.001	<0.0003	0.0026	0.0002	0.004	<0.01
C35MN6[1]	78.7	13	5.11	0.044	1.99	0.18	0.96	0.005	0.0003	0.0014	0.0002	<0.002	-
C35M01TC[2]	79.51	13	5.2	0.04	1.98	0.15	<0.01	0.024	<0.0003	0.0009	0.0004	0.002	0.08
C35M03TC[2]	79.34	13.03	5.17	0.04	1.97	0.15	<0.01	0.058	<0.0003	0.0009	0.0003	0.003	0.22
C35M10TC[2]	78.82	12.95	5.14	0.01	1.96	0.2	<0.01	0.18	<0.0003	0.0012	0.0007	<0.002	0.71

All other elements (Zr, B, Hf, V, W, Ce, Co, Cu, La, Mn, Ni) measured to be at or below <0.01
[1]VIM ingot, [2]Arc-melt and drop cast ingot

Once ingots were acquired and chemistry verified they were processed to produce the desired microstructure and mechanical performance. All alloy ingots were homogenized at 1200ºC in an argon gas atmosphere for 4 hrs for the VIM ingots and 1 hr for the arc melted ingots, followed by air-cooling and water-quenching. For VIM ingots, the ingots were then sectioned into small pieces. Sectioned VIM ingots and the arc melted ingots were then hot forged at 800ºC with total 50% thickness reduction to make plate-form samples. The plates were hot rolled at 800ºC with additional 40% thickness reduction (total 70% thickness reduction) and then subsequently annealed at 800ºC in laboratory air for 1 hr. The plates were warm-rolled at 300ºC with total 80% or 90% thickness reduction from the hot-rolled plates, and then annealed at 650ºC for 1 hr in air.

3.2 As-received Microstructural Observations

The base microstructure of the as-received conditions for the alloys in Table 1 has been reported previously [16, 17]. Optical micrographs of each alloy are shown in Figure 2. To summarize, all alloys showed a fully-ferritic microstructure under optical microscopy. The grain sizes and secondary phase distributions varied depending on the alloy type. The high Al-variants (C36M and C37M) showed elongated grains along the rolling direction with dispersions of partially recrystallized grains on the order of 5 µm. The C35MN alloys, as seen in Figure 2d, has Laves phase precipitate dispersions (the dark contrast particles) within a fine sub-grain structure while the alloys with TiC additions showed TiC precipitate dispersions (the dark contrast particles) within a fully recrystallized matrix with grain sizes near 10 µm. The volume fraction of the TiC dispersions seems to rise with increasing nominal TiC contents of the alloys, as can easily be expected.

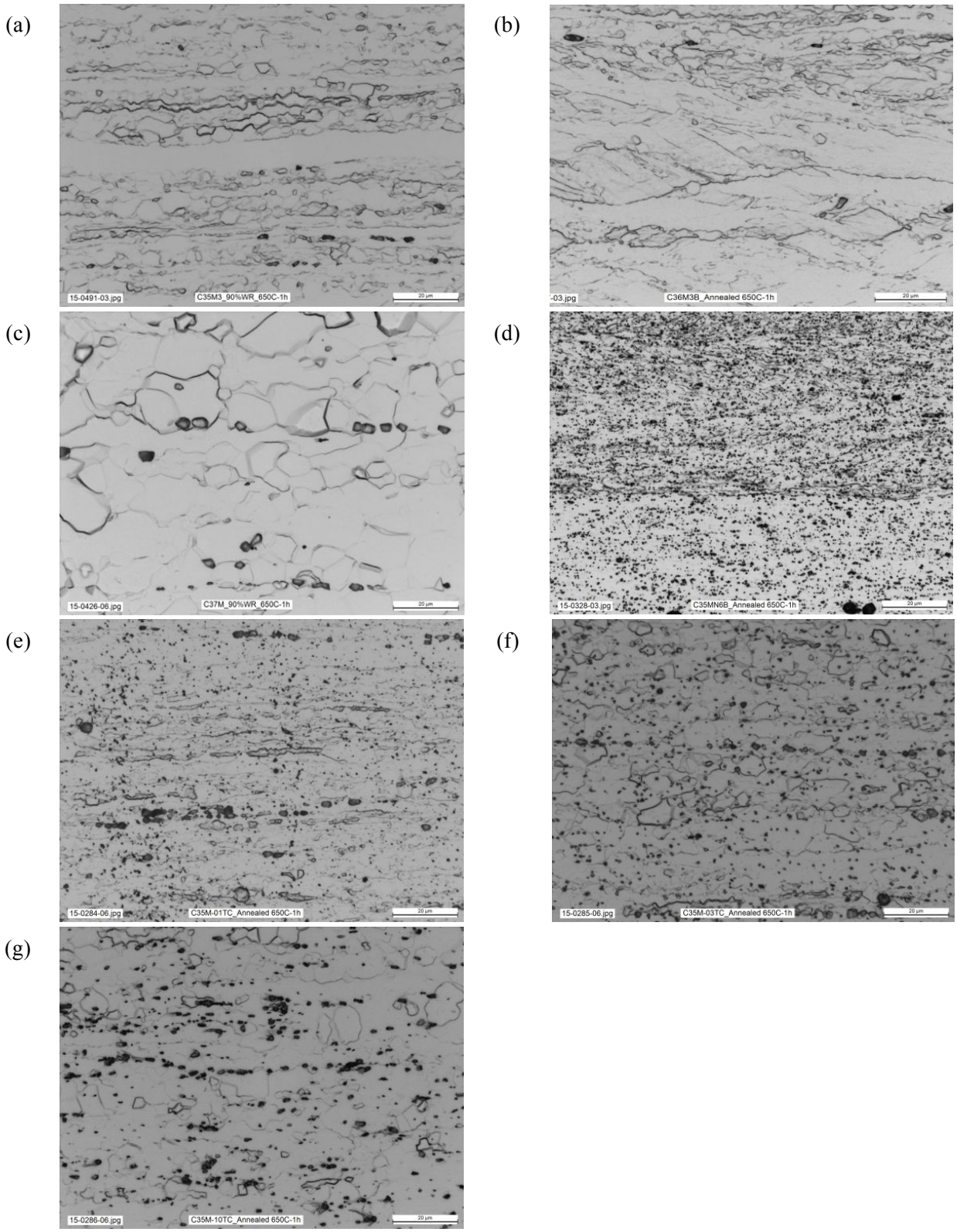

Figure 2: Optical micrographs of candidate FeCrAl alloys for welding and irradiation testing; (a) C35M, (b) C36M, (c) C37M, (d) C35MN, (e) C35M01TC, (f) C35M03TC, and (g) C35M10TC. Rolling direction is left to right in all images. Reproduced from Ref [17].

4. THERMAL AGING RESULTS AND DISCUSSION ON NON-WELDED SPECIMENS

4.1 Thermal Aging Test Conditions

Small samples with a nominal size of 400 mm x 400 mm x 0.75 mm were fabricated from the final sheet product for each alloy in Table 1. An additional set of alloys were fabricated and machined to evaluate the difference between model alloys versus the more complex alloys reported in Table 1. This was done to determine the effects of Mo, Si, Nb, and TiC on the thermal aging of FeCrAl alloys. These model alloys were processed to have grain size control by a combination of hot-rolling with more than 90% total thickness reduction at 700ºC and subsequent annealing in a temperature range between 700-750ºC, resulting in a uniform, equiaxed grain structure with grain sizes in a range of 30-80 μm [5]. The compositions of the model alloys are listed in Table 2. These model alloys were determined to have a fully ferritic grain structure with grain sizes between 30-80 μm. Neither the model nor candidate alloys had their surfaces prepared prior to thermal exposures. All specimens were laser engraved prior to heat treatment with unique identifiers to ensure proper specimen tracking.

Table 2: Model FeCrAl alloys composition in weight percent added to the test matrix for thermal aging experiment test matrix.

Alloy	Fe	Cr	Al	Y	Mo	Si	Nb	C	S	O	N	P	Ti
T35Y	82.26	13.18	4.44	0.07	<0.01	0.01	<0.01	0.0040	0.0009	0.0022	0.0026	0.009	<0.01
B136Y	80.85	12.99	6.14	0.003	<0.01	<0.01	<0.01	0.0030	0.0020	0.0014	0.0005	<0.002	<0.01
B137Y	80	13	6.98	0.003	<0.01	<0.01	<0.01	0.0040	0.0018	0.0013	0.0002	<0.002	<0.01
B166Y	77.86	16.06	6.06	0.003	<0.01	<0.01	<0.01	0.0030	0.0023	0.0014	0.0004	<0.002	<0.01

All other elements (Zr, B, Hf, V, W, Ce, Co, Cu, La, Mn, Ni) measured to be at or below <0.01

After machining, samples were placed in calibrated box furnaces at a temperature of 400°C or 475°C to determine the temperature effects on thermal aging of FeCrAl alloys. The thermal heat treatment was conducted in air. It was considered that the good oxidation resistance of FeCrAl alloys in air did not necessitate a protective atmosphere; additional surface preparation was completed to mitigate any issues with an interaction layer. Samples were placed in each furnace for 1, 4, 8, 24, 100, 500, and ~1000 hrs. Another set of samples is currently still being heat treated at both temperatures with an expected removal time of 5000 hrs. These samples will be removed in early February 2016. Samples up to ~1000 hrs were removed from the furnaces and allowed to air cool. Samples were then metallographically prepared to a final polish of 1200 grit or better to remove any surface oxidation layer or abnormalities from specimen machining. The same surface preparation was completed on as-received (non-aged) samples.

Hardness testing was completed in accordance with ASTM E384: *Standard Test Method for Knoop and Vickers Hardness of Materials* using a Wilson VH3100 model microhardness indenter. A Vickers indenter tip was used with an indent load of 300 g with a dwell time of 10 s. Fifteen indents were completed at random locations for each sample and condition, those that did not meet requirements of the ASTM E384 standard were removed from the dataset and the mean and standard deviation was recorded. Currently, the C35M01TC, C35M03TC, and C35M10TC have not been evaluated due to time restrictions but will be included in the final dataset.

4.2 Observations and Results

Figure 3 shows the increase in hardness values (ΔHv) after thermal aging at 400°C and 475°C up to 1200 hrs for the candidate and model FeCrAl alloys. It can be seen up to 100 hrs, limited changes in the

hardness values were observed in any alloy aged at either investigated temperature. This result agrees with similarly reported changes in hardness for FeCr alloys [18]. At and above 100 hrs, an increase in the hardness is observed in the candidate alloys (C-series) for both temperatures but only observed in the T35Y and B166Y alloys for the model alloys. When observing the ΔHv above 100 hrs for both alloy series, Al additions tended to decrease the ΔHv, a result within agreement for recent studies on FeCrAl alloys aged at 475°C [11]. For the model alloys, Cr content also played a role in the observed ΔHv, with the highest Cr alloy (B166Y) showing significant hardening at 400°C compared to the 13 wt.% Cr FeCrAl alloys. Comparing the candidate FeCrAl alloys (C-series) with the model alloys (B and T series) with the same Cr and Al content it appears that the C-series, with Mo and Si additions, have increased hardening compared to the model alloys aged at the same time and temperature.

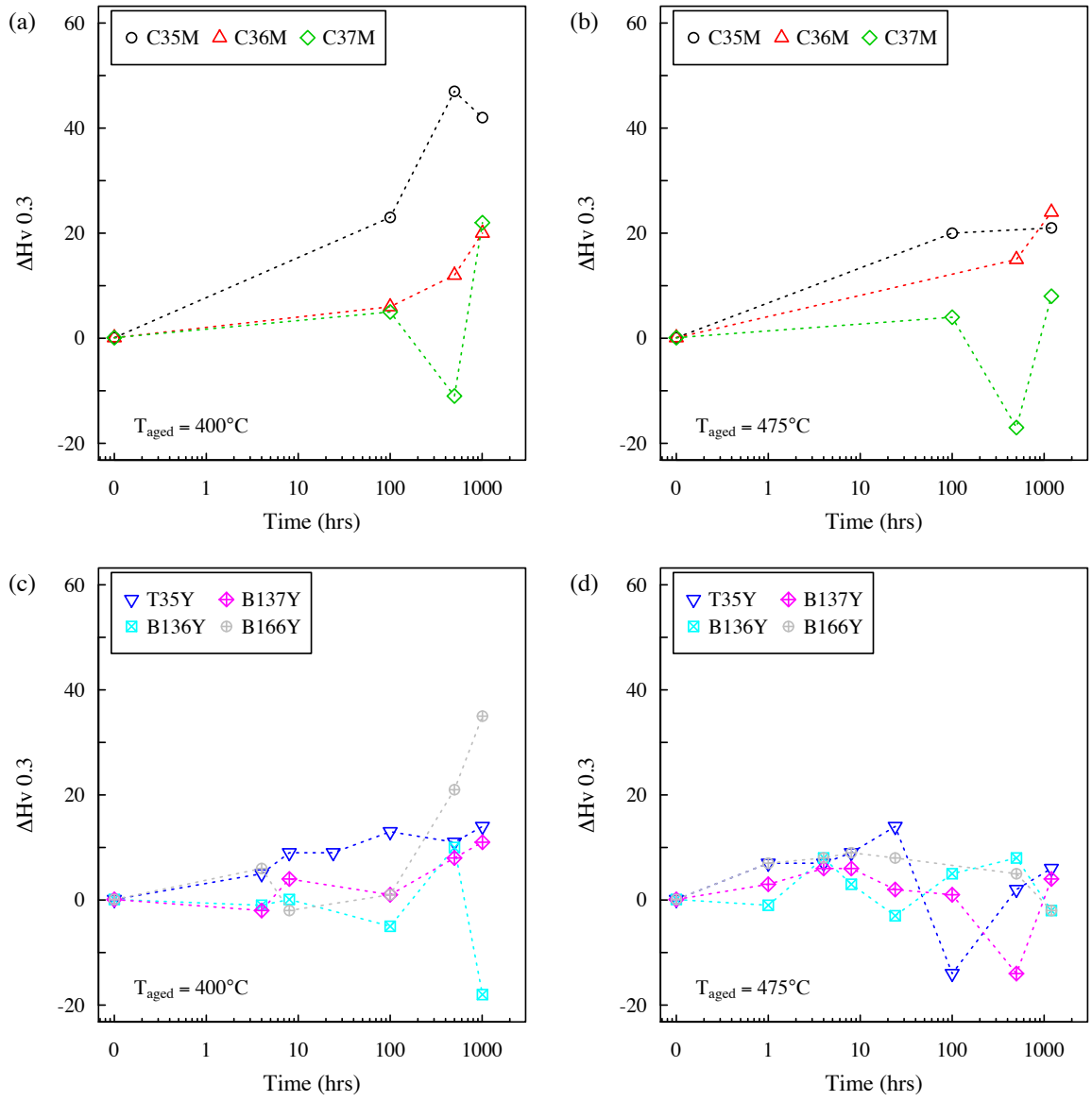

Figure 3: The effect of Cr and Al addition on the change in microhardness in candidate FeCrAl (a & b) and model alloys (c & d) as a function of time at (a & c) 400°C and (b & d) 475°C. Data points are based on averaging greater than 5 individual measurements, standard deviations were on average 4-5 Hv 0.3.

The results shown in Figure 3 suggest competing factors in the phase stability of FeCrAl alloys including Cr composition, Al composition, minor solute addition, time, and temperature effects. For FeCr and FeCrAl alloys, the hardening responses have been directly linked to the precipitation of the Cr-rich α' phase (See Refs. [3, 11, 19-21] and those within). The results here indicate a time dependence for the precipitation of α', where at low aging times (<100 hrs) no ΔHv is observed. It can be hypothesized that at these low aging times the Cr-rich α' phase has not reached significant volume fractions to lead to hardening for the alloys investigated in this study. This would be in agreement with other studies where the strengthening of the Cr-rich α' in the matrix has been modeled using the dispersed barrier model and indicated that a critical size and number density must be reached before observing any significant mechanical property change [3, 22]. This effect is due to Cr-rich α' being a weak barrier to dislocation motion under deformation and hence significant volume fractions are needed.

The major alloying addition effects (Cr and Al) can be rationalized based on the phase diagram proposed by Kobayashi and Takasugi [11] for the FeCrAl ternary phase diagram developed from a similar thermal aging study. There, Kobayashi and Takasgui showed Al in solid solution can lead to the suppression of the phase separation of the α-phase to the Fe-rich α phase and the Cr-rich α' phase. Here, the 13 wt.% Cr alloys straddled the defined α – α' phase boundary by Kobayashi and Takasugi at 475°C taking into consideration the experimental error of their study. Thus, it would be expected that as the closer the composition reaches the phase boundary, such as the C36M and C37M alloys, a reduced volume fraction of the Cr-rich α' phase would precipitate leading to a reduced hardening response as seen in our study. The same principles follow between the B136Y and B166Y samples at 475°C, where the B166Y samples falls just outside of the phase boundary at 475°C. The 400°C response for the B166Y (16 wt.% Cr) is to be expected. The results of Bonny et al. [12], proposed a FeCr phase diagram based on experimental work that indicates at temperatures above 450°C, higher Cr contents can be accommodated while negating the formation of α'. Here, the results suggest the 16 wt. % Cr, 6 wt. % Al alloy falls within the phase boundary at 400°C but does not at 475°C due to a similar phase boundary temperature effect for FeCrAl alloys as in the FeCr alloys.

The significantly higher hardening values and apparent increased rate of hardening in the candidate alloys is in agreement on several reports for FeCr alloys [19, 21]. These reports indicated that at the aging temperatures near 475°C, Mo and Si can intensify the hardening of FeCr alloys when the compositions are remained relatively low in the FeCr matrix. Several mechanisms have been proposed for this intensifying feature including that substitutional elements such as Mo and Si could increase the lattice parameter of α' and thus the internal strains within the alloys after precipitation or could act as a promoter of the nucleation of α' by forming carbides in the alloys [19, 21]. For the C-series alloys studied, the secondary mechanism (increased sites for heterogeneous nucleation) seems unlikely as the alloys studied had very low C contents (<0.005 wt. %, Table 1) meaning limited abilities for the formation of carbides during heat treatment. Another mechanism is the Mo and Si could adjust the thermodynamics of the system leading to a shift in the phase boundary towards lower Cr contents, particularly at 475°C. This could be a possible reasoning for contrast between Figure 3b and Figure 3d. Clearly, the results shown in Figure 3 for the candidate FeCrAl alloys warrant further investigations to confirm or deny the proposed mechanism(s) leading to the increased rate of hardening in these alloys.

4.3 On-going and future work

The results provided in Section 4.2 provide a base understanding on the factors for α – α' phase separation in FeCrAl alloys for nuclear power production. This is especially important when comparing and contrasting to upcoming post-irradiation examination (PIE) results. By establishing the trends in the unirradiated state, it can better inform on whether radiation enhances the phase separation in FeCrAl alloys. To continue developing the understanding and assist with PIE analysis, further work is needed. The first priority is to complete hardness testing evaluations on the candidate FeCrAl alloys with TiC

additions to determine if the additions retard or enhance the observed phase separation and compare and contrast the results to the already observed alloys. Furthermore, several of the data points in Figure 3 seem to show significant softening, these data points need further investigation. As stated in Section 4.1, an additional set of samples are being aged up to 5000 hrs. These samples will be tested to determine the long-term aging response of the candidate and model alloys. Finally, selected samples will have more robust microstructural characterization completed, including the determination of the size, volume fraction, and number density of α' precipitates using advanced electron microscopy techniques.

5. HYDROGEN CHARGING RESULTS AND DISCUSSION ON NON-WELDED SPECIMENS

5.1 Parameters and design of systems

Two techniques are currently in development to complete hydrogen charging of candidate FeCrAl alloys. These techniques are being used in lieu of welding in hydrogenated atmospheres as they can generate precise and repeatable concentrations in bulk of the FeCrAl alloys. Such precision with repeatability is needed for eventual mechanical testing where several specimens with the same hydrogen content must be tested to provide a statistical average. The best technique will then be used to determine the confluence between microstructure, chemistry, and hydrogen-induced cracking during welding on the candidate FeCrAl alloys. Details on the static gaseous charging system and initial results have been previously published [16, 23] but is reported here for completeness.

5.1.1 Static gaseous charging

The static gaseous charging system used here is shown schematically in Figure 4. The system consists of a three-zone tube furnace (maximum temperature of 1100°C), a 304SS process tube, a hydrogen generator, a vacuum system, and an argon gas supply. The system is controlled and monitored using digital controls. The gas generator used in this system is capable of producing a constant stream of hydrogen with a maximum gas flow rate and pressure range of 260 cc/min and 0.13-0.79 MPa, respectively. Test FeCrAl samples were placed in a high purity alumina boat, which was inserted into the process tube. Multiple high purity Ar purges gave rise to a nearly oxygen free environment. Prior to heating, a controlled amount of hydrogen was introduced into the closed system and then the system was brought up to temperature. The hydrogen uptake by using this technique is determined by the intrinsic hydrogen solubility and the equilibrium hydrogen pressure in the materials of interest.

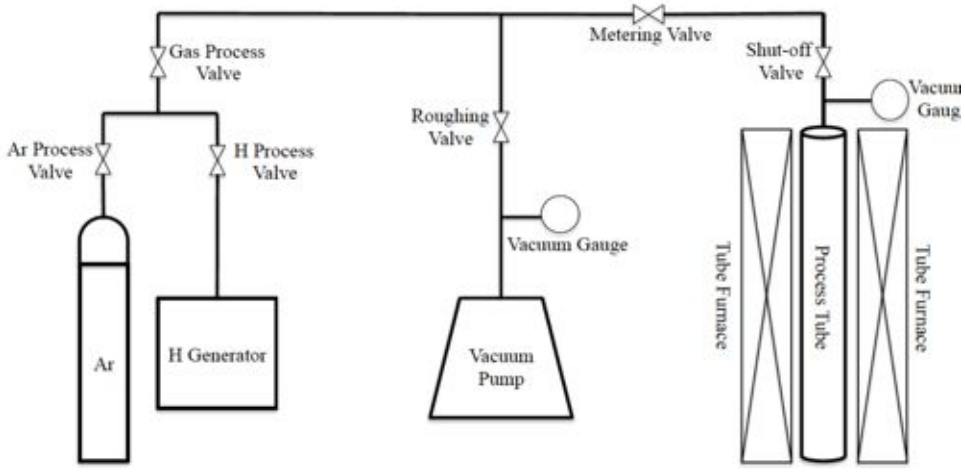

Figure 4: Schematic illustration of the gaseous hydriding system at ORNL.

5.1.2 Cathodic charging

The schematic plot of the cathodic hydrogen charging system is shown in Figure 5. Cathodic charging was carried out in a solution of 0.1N sulfuric acid, containing 0.25 g/L sodium arsenite powder (readily soluble in sulfuric acid) as a hydrogen recombination inhibitor. Pt wires were used to connect the specimens and the Pt anodes (Pt mesh) to the DC power supply. In order to have a good contact, the Pt wires were welded directly to the Pt mesh anode and the specimens by using an electric resistance welding technique. The B&K Precision high-resolution DC power supply is capable of a maximum output with 30 V and 1 A. The charging current density employed was in the range of 50-200 mA/cm^2. The hydrogen content in the samples following the charging process is determined by a combination of several factors, including charging current, charging time, the solution temperature, and the sample geometry. Given the high mobility of hydrogen in steels at room temperature, a fast hydrogen release from the charged samples is expected when transferring the charged specimen to the LECO analyzer for hydrogen determination (Section 5.1.3). Therefore, a small Dewar filled with liquid nitrogen was used as the transportation tool to mitigate the hydrogen release. Note that a shortcoming of this technique is that the relatively small diffusion distances obtained during a laboratory-scale cathodic charging process leave the hydrogen transport limited to the near surface [24]. Alternatively, the cathodic charging process could be attempted on FeCrAl alloys in a flat and thin shape to ensure a relatively uniform hydrogen distribution throughout the sample thickness.

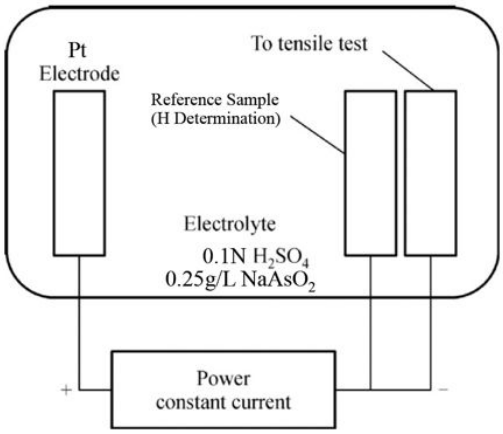

Figure 5: Schematic illustration of the cathodic charging system at ORNL.

5.1.3 Hydrogen content determination

A LECO® OH836 oxygen and hydrogen analyzer was used after the hydrogen charging process to determine the hydrogen content. This instrument uses an inert gas fusion technique to complete the analysis. This technique involves the placing of the sample in a high purity graphite crucible held between electrodes in an impulse furnace, where after inert gas (helium) purging cycles, current is applied to the crucible rapidly heating the sample. During the process, gas (oxygen and hydrogen) is released from the sample, with oxygen reacting with the graphite crucible to form CO and CO_2. Released gas from the sample is picked-up by the flowing inert gas and passed through a heated reagent where the CO is oxidized to CO_2 and H_2 is to H_2O. The CO_2 and H_2O are detected using non-dispersive infrared cells. The CO_2 and H_2O absorb infrared energy at unique wavelengths, with the concentration of the gases compared to determined values from a calibration standard. The measurement limits for hydrogen and oxygen are 0.1 ppm to 2500 ppm and 0.05 ppm to 5.0% for a 1 g sample, respectively.

5.2 Effect of Hydrogen Charging

5.2.1 Static gaseous charging

Two different trials were run on the C35M, C36M, and C37M samples to determine the viability of using the static gaseous charging system for full scale testing. The two trials used varied temperature profiles, the first used a profile of 20 min to 200°C, 80 min to 600°C followed by 12 hrs at 600°C while the second trial used a slightly more elevated temperature profile of 20 min to 200°C, 100 min to 700°C, and 6 hrs at 700°C. The initially introduced hydrogen amounts were 250 torr and 400 torr, respectively. The resulting hydrogen and oxygen content after these two trials for the three different alloys are provided in Table 3. Table 3 indicates no significant changes in either the oxygen or hydrogen content of the alloys after the two-hydriding processes. The low oxygen content also indicates no oxides were formed during the high temperature hydrogen charging process. The results in Table 3 indicated that the static gaseous charging process based on the current system was not a viable process for conducting controlled testing on the effects of hydrogen on the mechanical properties of FeCrAl weldments. It is emphasized here that static gaseous charging actually is a very effective way to introduce homogeneous hydrogen distribution to steels [25]. However, it requires extremely high hydrogen pressure (in a level of GPa) and high temperature. Due to the limitation of the current gaseous hydriding system and safety concerns, we will not pursue high-pressure hydrogen charging for this project.

Table 3. Oxygen and hydrogen contents after the two gaseous hydriding processes and the cathodic charging. The oxygen and hydrogen of as-received samples are also listed for comparison.

Sample ID	As-received			Static Gas-phase charging (Trial 1)			Static Gas-phase charging (Trial 2)			Cathodic H charging (200mA/cm^2, 48 h)		
	Mass (g)	O (wppm)	H (wppm)	Mass (g)	O (wppm)	H (wppm)	Mass (g)	O (wppm)	H (wppm)	Mass (g)	O (wppm)	H (wppm)
C35M	0.118	110	1.39	0.134	63.9	2.81	0.1553	69	2.49	0.135	116	24.5
C36M	0.104	151	3.98	0.126	82.6	2.27	0.1695	110	1.69	0.137	130	21.3
C37M	0.103	171	3.72	0.100	61.8	1.96	0.1617	117	2.34	0.144	111	25

5.2.2 Cathodic charging

Tentative measurements were conducted by employing the cathodic hydrogen charging system for C35M, C36M, and C37M. The charging electrical current was set to be 200 mA/cm^2 with a charging time of 48 hours at room temperature. The measured hydrogen contents for these three samples are also shown in Table 3. It is apparent that the hydrogen contents in materials after cathodic charging are around 10 times higher in comparison with the as-received samples. Moreover, the similar results for these three samples indicate that the composition difference (5~7wt.% Al) did not impact the hydrogen uptakes significantly. It is expected that higher charging current and longer charging time will lead to even higher ultimate hydrogen content. Therefore, the preliminary results gave us confidence to use the cathodic hydrogen charging method to continue the investigation of hydrogen effects on FeCrAl alloys and weldments under well-controlled experimental conditions.

5.3 On-going and future work

Given the fact that static gas-phase hydrogen charging based on the current experimental setup is not viable for the proposed work, cathodic hydrogen charging method will be centered on to introduce various hydrogen contents to the studied FeCrAl alloys in a well-controlled way. First, it is necessary to identify the cathodic hydrogen charging conditions (e.g., charging time and current) for different hydrogen contents required. Good repeatability is critical to the eventual mechanical testing. Second, the impact of the inclusion of TiC on the hydrogen uptakes in FeCrAl alloys will be evaluated by conducting

a series of cathodic hydrogen charging experiments for the samples without TiC under the same charging conditions. Finally, tensile tests will be performed for the post-charged specimens to assess the hydrogen effects on the mechanical properties of FeCrAl alloys and the weldments.

6. WELDABILITY RESULTS AND DISCUSSION

6.1 Preliminary welding trials

The base alloy, C35M, was used to perform the preliminary welding trials to find optimized laser weldeding conditions. Prior to welding, the sample was cleaned of surface oxides and contamination. A pulsed laser-beam-welding (LBW) machine was used to perform autogenous, bead-on-plate welding. Conditions were optimized to perform a full penetration weld. No pre-heating of the specimens was used and an inert argon cover gas was used during welding. Full penetration was found at welding parameters of 7 ms pulse length, 7 pulses/s and 2.12 mm/s welding speed. Lamp energy was maintained to have a nominal average of 100 Watts. Post-welding inspections included routine visual inspections and a high magnification optical inspection using a Keyence VHK-1000 confocal optical microscope. Extensive post-weld characterization was not completed on the preliminary samples, as the goal of this trial was to achieve optimized parameters for full penetration. All welds were performed in the traverse direction.

6.1.1 Observations and results from preliminary welding trials

The preliminary welding trials on C35M were inspected optically to determine the viability of using the optimized parameters for LBW for full penetration weldments. Visual inspection showed the weldments had no cracking, porosity, or other surface anomalies, as seen in Figure 6a. Several specimens were extracted from these preliminary weldments to perform initial tensile testing on the welds to determine the strength. Upon pre-testing inspection, the specimen profiles showed a depression in the fusion zone, Figure 6b. It was speculated that the depression in the fusion zone is most likely due to limited cooling during the welding procedure leading to extended melting of the fusion zone and the observed depressions. A secondary batch of preliminary welding was completed where care was taken to increase the cooling rate of the weldment that leads to significant reduction or complete elimination of the depression in the fusion zone of the weldments. Based on these preliminary weld trials, the parameters and conditions for LBW of the candidate FeCrAl alloys were set, and more extensive welding trials were completed on all alloys.

a) b)

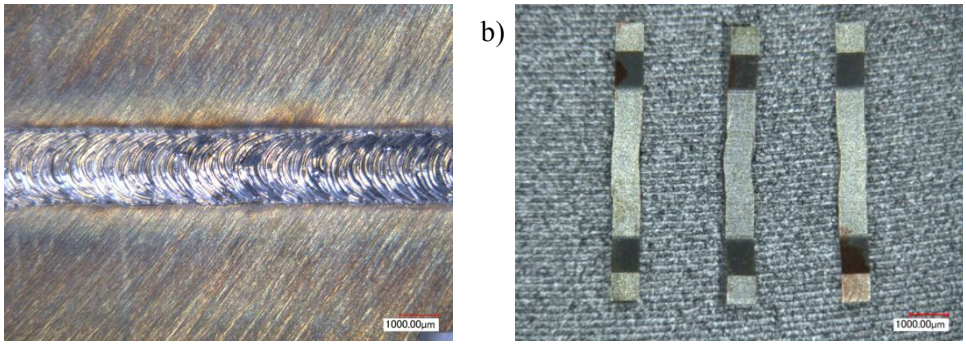

Figure 6: Optical micrograph of the traverse laser weld on the top (incident) surface showing no signs of cracking or surface defects in the specimen.

6.2 Optimized welding trials

Details on the completed optimized welding trials can be found in a previous report of this program [17]. To summarize, the same optimized welding parameters used in the preliminary welding trial on C35M was conducted for all other candidate alloys. The C35MN weld, due to being thicker sheet product, required an elevated laser power setting to achieve full penetration. For all welds, care was taken to increase the cooling rates after welding to limit the depression zone in the fusion zone. All welds were performed in the traverse direction (perpendicular to the rolling direction). Samples for microscopy and characterization were taken from the lot of specimens used for the building of the irradiation targets for the High Flux Isotope Reactor (HFIR) irradiations. Specifically, the left over material between the SS-J2 tensile bars, which forms an oval shape, was used. Samples after welding were mounted in epoxy and prepared metallographically to mirror finish with colloidal silica polishing as the last step to provide a cross-sectional view of the microstructure in the fusion zone, heat-affected zone, and the base materials.

Scanning electron microscopy coupled with electron backscattered diffraction (SEM-EBSD) was used for grain size, orientation, and shape quantification as well as analysis of cracks and/or inclusions. SEM-EBSD was performed using a JEOL JSM 6500F microscope with a field emission gun (FEG), equipped with an EDAX EBSD system. The accelerating voltage was 20 kV, and the working distance was 12 to 17 mm. EBSD maps were measured on a hexagonal grid with a step size of 0.5 to 3.0 μm. The camera operated in 2×2 binning mode at ~90-100 frames per second (fps). These parameters were chosen to keep the EBSD analysis time within reasonable limits taking into account the large size of the scanned areas.

6.2.1 EBSD analysis of candidate FeCrAl alloys after optimized welding

In this section, the structure of the advanced FeCrAl alloys prior and after welding will be discussed in detail using the results of the SEM-EBSD analysis. The grain reference orientation deviation (GROD) parameter will be used as a criteria to separate recrystallized and non-recrystallized grain fractions. GROD shows the misorientation of a point from the average grain misorientation. Larger GROD usually corresponds to larger plastic strain within the grain. Image quality (IQ) maps will be employed as a convenient and informative way to give a qualitative description of the structure. Note that all inverse pole figure (IPF) maps in the present section are colored with respect to the rolling direction during the final warm-rolling step.

6.2.1.1 The structure of parent materials

6.2.1.1.1 C35M alloy

Figure 7 shows a typical view of the sample after the final polishing step with colloidal silica. One can see a clean, exceptionally flat surface (Figure 7a) without any mechanical damage or any other obvious defects like pores or scratches. High magnification view (10000×, Figure 7b) revealed small particles with a size of ~0.2 μm or less. Some of the particles were embedded in the surface and believed to be carbides. Some particles were caused, most likely, by carbon coating. Additionally, inclusions of round shape with a size of ~1-5 μm were observed in the structure (black arrows in Figure 7b). The inclusions had clear visible boundaries after mechanical polishing with colloidal silica; their surface level, as a rule, was slightly below the sample surface suggesting lower hardness compared to the parent material matrix.

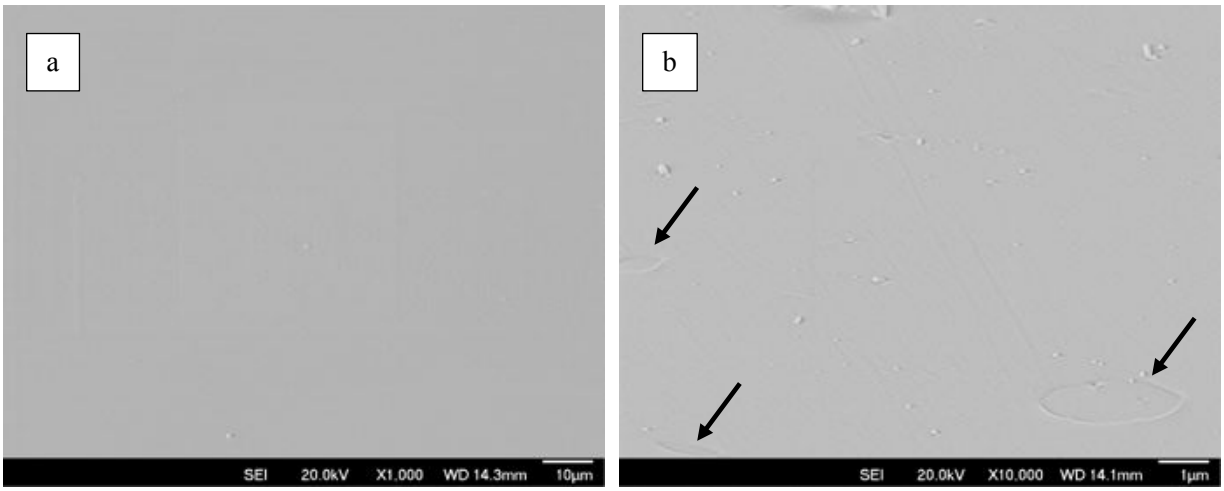

Figure 7: Typical SEM images of the specimen surface (tilted at 70°). Final preparation step was mechanical polishing with colloidal silica; carbon coating was employed to avoid charging during specimen analysis in the SEM. Black arrows point to a few inclusions in the structure.

Prior to EBSD scanning, the specimen surface was analyzed with optic and SEM in the magnification range of 100-1000×; no cracks or other welding-induced defects were observed. Such appearance of the surface was typical for all analyzed alloys. No systematic differences or peculiarities were observed between specimens with only minimal variations in the inclusion density and morphology.

Figure 8 shows the structure of C35M alloy prior to welding. The structure consisted of warm-rolled material, which has elongated, fragmented grains with pronounced texturing, and recrystallized material with small grains of equiaxed, rounded shape. EBSD observations of grain morphology are in agreement with the optical observations in Section 3.2. The warm rolled material looked like dark-gray lines or bands in the IQ maps and had significant in-grain misorientation level (see GROD map in Figure 8a). Recrystallized grains had much lower GROD value and light-gray color in IQ maps with clear, well-visible grain boundaries. The re-crystallized grains formed specific chains elongated in the rolling direction. The layers of non-recrystallized and recrystallized materials alternated within the structure forming a specific band-like structure.

In the C35M alloy, the volume fractions of recrystallized and non-recrystallized material were close enough. However, some spots with a domination of round-shape grains were observed, Figure 8b. Such spots had no bands of warm-rolled material. Judging by the GROD values, the spots did not experience full recrystallization. The GROD values there were up to ~19-20° (Figure 8b) compared to the ~25° inside the warm rolled bands, Figure 8a. Most likely, such specific areas appeared due to the local differences in the recrystallization processes; the bands were consumed first forming a larger number of small grains. The reasons, which led to the different recrystallization kinetics and formation of such spots, are not clear at the moment.

Instead of the annealing and particular recrystallization, the alloy had strong rolling texture, Figure 9. Grains oriented close to the [101]-corner dominated the structure (up to ~5.5×random). Inclusions of round shape with a size of ~5-10 µm were observed in the structure. The inclusions were not identified; no acceptable-quality EBSD patterns were obtained for these inclusions.

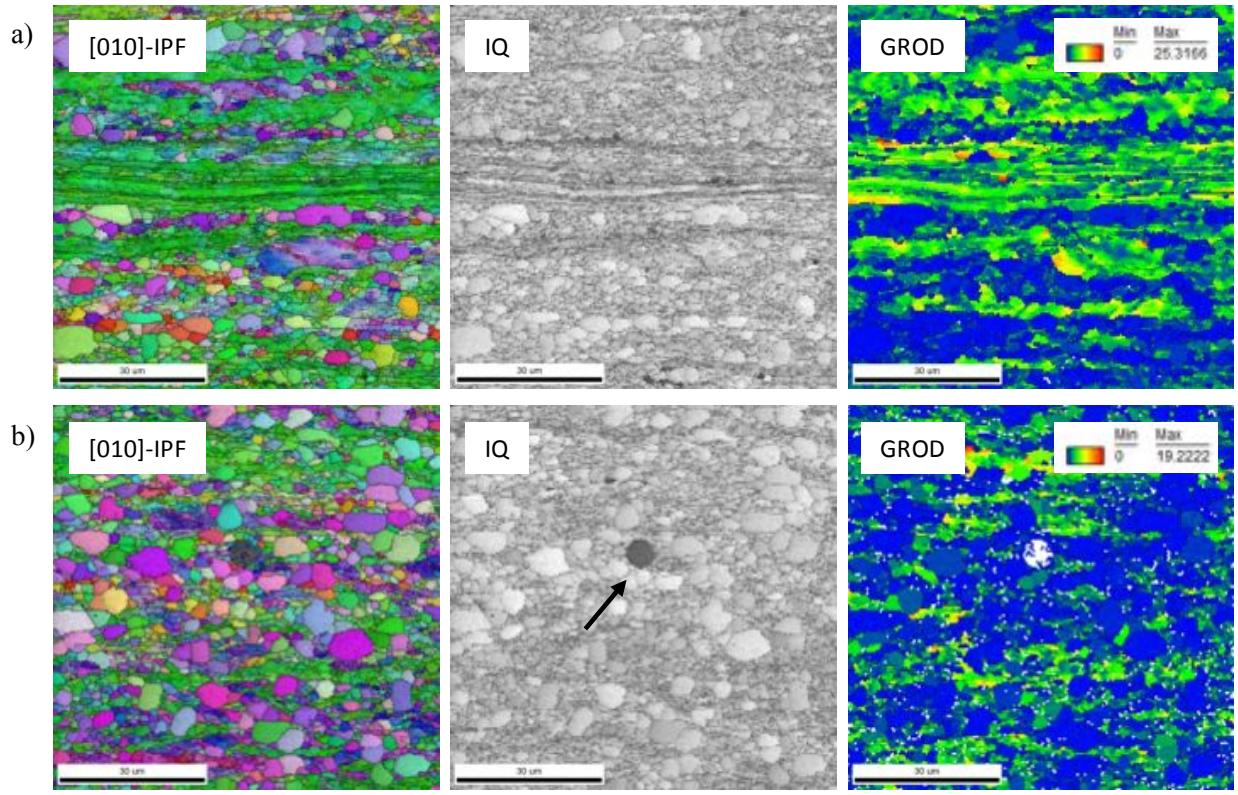

Figure 8: EBSD data from parent material of C35M alloy, a) typical partly recrystallized area and b) typical area with recrystallized grains. Black arrow points non-identified inclusion in the structure.

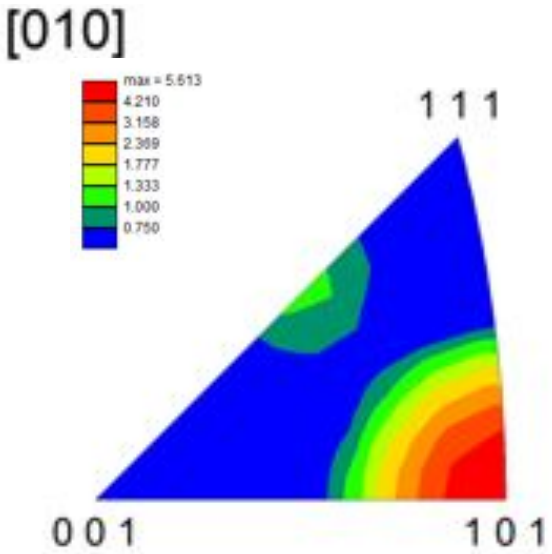

Figure 9: The texture of C35M alloy prior to welding.

6.2.1.1.2 C37M alloy

Figure 10 shows the typical structure of the C37M alloy. Compared to the C35M, discussed above, the aluminum content in this alloy was increased from 5.2 to 7 wt.%, Table 1, but their processing routes and final annealing modes were identical. As follows from the images, the structure consisted of recrystallized grains with low GROD parameter (blue color in the GROD map, Figure 10) and retained banding of warm-rolled material with fragmented grains. In the last case, the GROD value reached ~20° and these bands had pronounced texturing (green color in the IPF map). Interestingly, the fraction of the non-recrystallized material was significantly smaller in this alloy compared to the C35M.

In some cases, the structure also contained small line-like defects, most likely non-metallic inclusions. The inclusions ("stringers") were elongated in the rolling direction. As believed, these defects were caused by the material processing routes, Section 3.1.

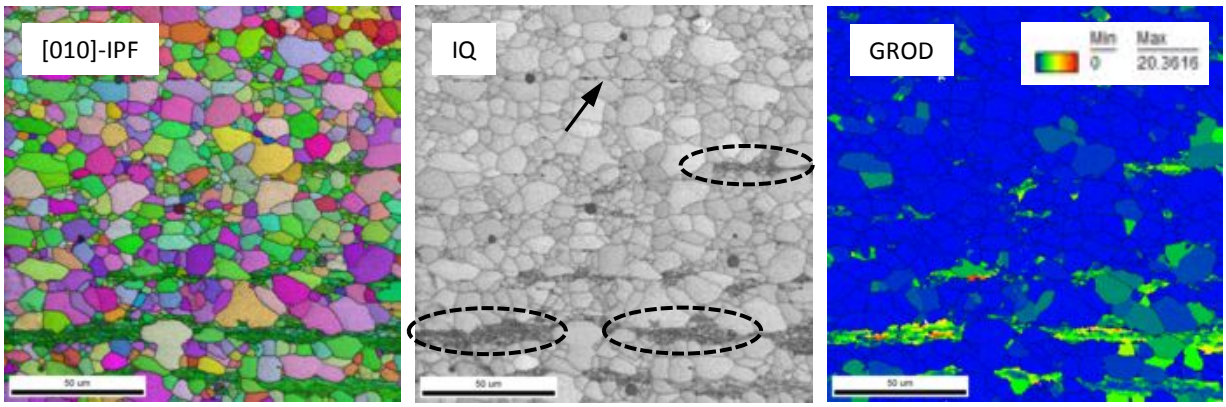

Figure 10: Typical structure of the C37M alloy. Black dashed ovals show non-recrystallized areas. Black arrow shows elongated defect ("stringer").

6.2.1.1.3 C35M01TC alloy

The composition of the C35M01TC alloy was identical to the C35M alloy except the addition of titanium carbide (TiC, nominally 0.1%). The non-welded material structure is shown in Figure 11; as follows from the image, the structure consisted of recrystallized and non-recrystallized grains. The size of recrystallized grains was close to that of the C35M alloy, Section 6.2.1.1.1. Interestingly, the GROD values for these materials also were close enough (~25° and ~22° for C35M and C35M01TC, respectively).

Light scratches were observed at the surface (Figure 11, IQ map), even though the same polishing procedure was used for the C35M01TC alloy as the pristine surface of the C35M and C37M alloys. The scratches were not visible in the SEM images, but the IQ maps revealed them distinctively. Most likely, the scratches were caused by TiC-particles that had fallen from the metal matrix during the final preparation step. Since the carbides were the part of the alloy, it was impossible to eliminate the scratches completely.

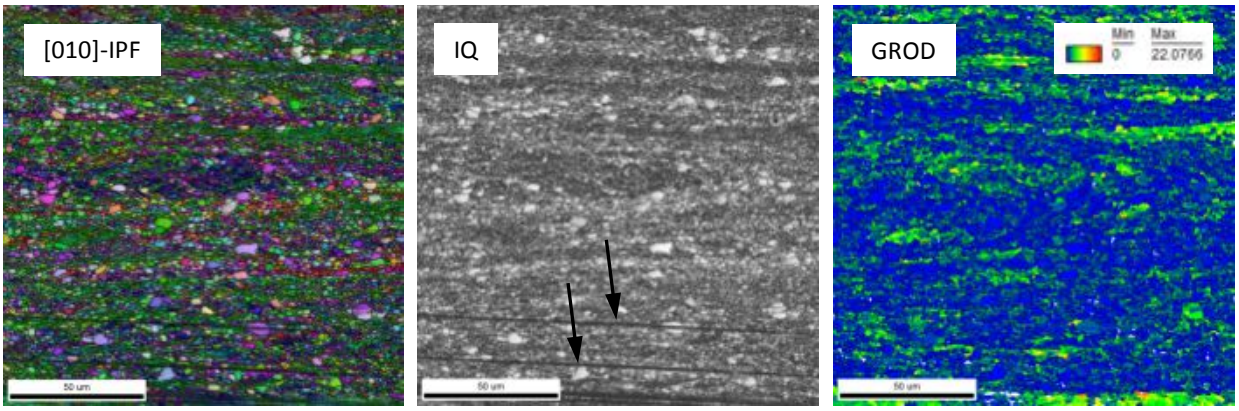

Figure 11. Typical structure of the C35M01TC alloy. Black arrows point to a few well visible scratches.

6.2.1.1.4 C35M03TC alloy

The C35M03TC alloy had the structure similar to the C35M01TC in many aspects, Figure 12. The structure consisted of recrystallized and non-recrystallized fractions of comparable volume. The size of recrystallized grains was also similar. No specific peculiarity was observed in this alloy compared to the materials analyzed before.

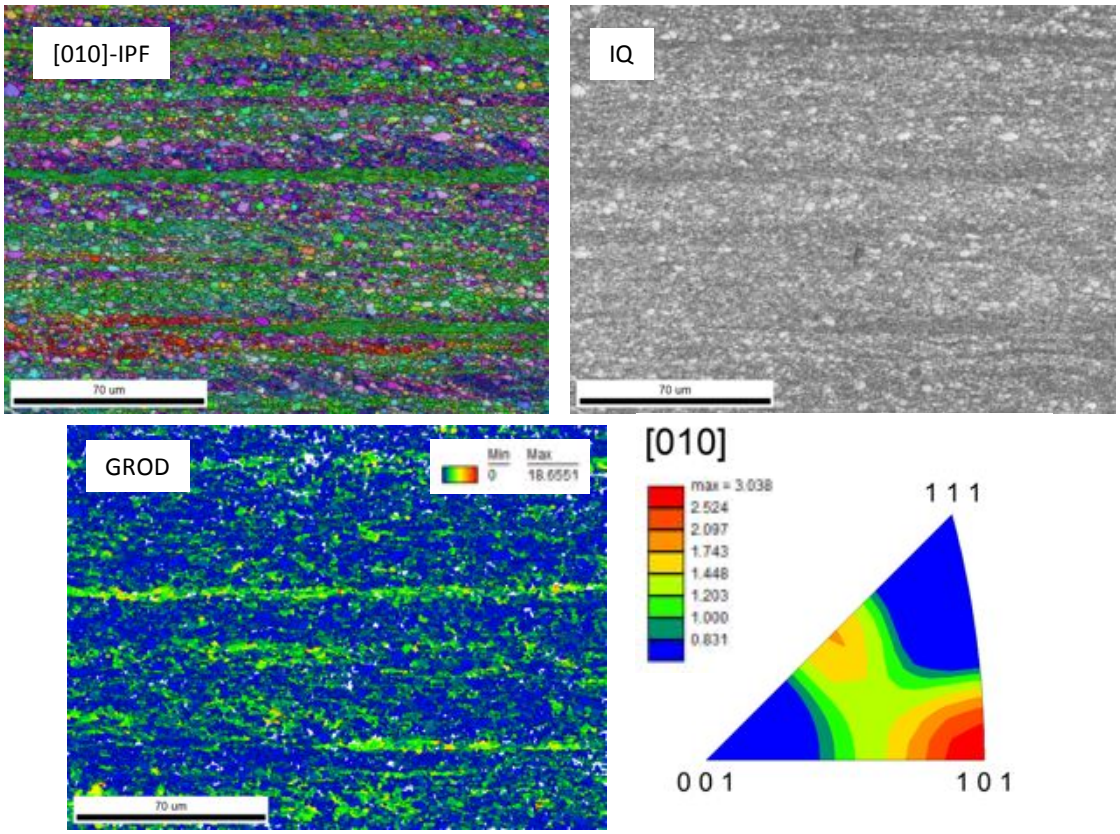

Figure 12: Structure of the C35M03TC alloy.

6.2.1.1.5 C35M10TC alloy

Figure 13 shows the typical structure of the C35M10TC alloy. The structure of this alloy is close to the other materials. One may see a combination of recrystallized and non-recrystallized areas. The size of recrystallized grains was also similar to the C35-family alloys discussed above. The GROD value is close enough (~25°) to the other materials. No new details or peculiarities were observed due to the nominal 1 wt.% TiC addition.

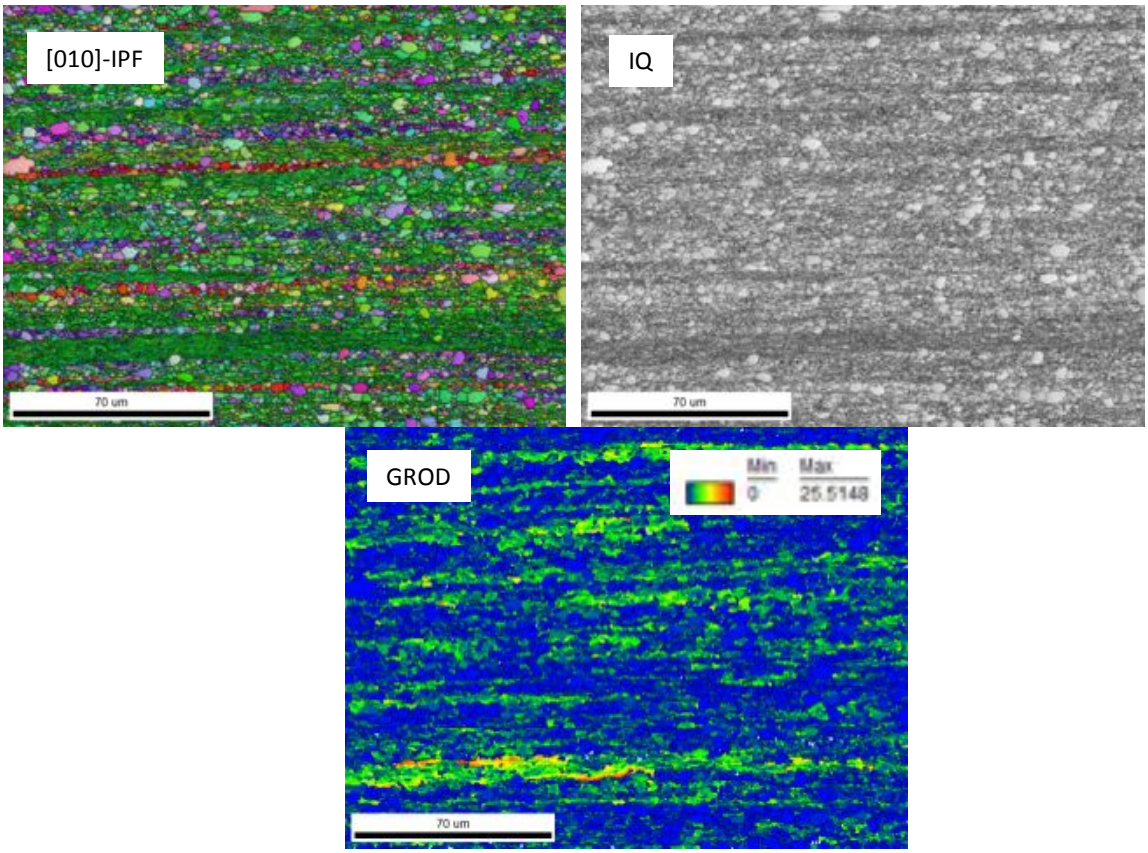

Figure 13: Structure of the C35M10TC alloy in the non-welded area.

6.2.1.2 Post-welding structure

In this present section, the structure of the materials after welding will be discussed in detail. The focus will be made on the C35M alloy since this material served as a base for the following modifications. For the rest of materials, a limited description will be given with emphasis on the alloying impact on the structure before and after welding.

6.2.1.2.1 C35M alloy

Figure 14 shows the stitched image of the weldment. To compose the image and analyze the structure in detail, up to 6-8 EBSD scans were performed at low magnification (100×). Low-magnification scans allowed for the scanning of the entire specimen thickness (~0.8 mm) but led to some image distortion that was especially pronounced at the scan edges. The distortion may influence the calculation of grain size but cannot influence the general structure morphology.

Welding led to the formation of relatively large grains of irregular shape near the weldment centerline, Figure 14. Starting ~300-400 μm from the centerline, elongated or columnar grains dominated the structure suggesting strong thermal gradients. The width of the columnar grain area was ~300 μm, and this value varied slightly through the specimen thickness.

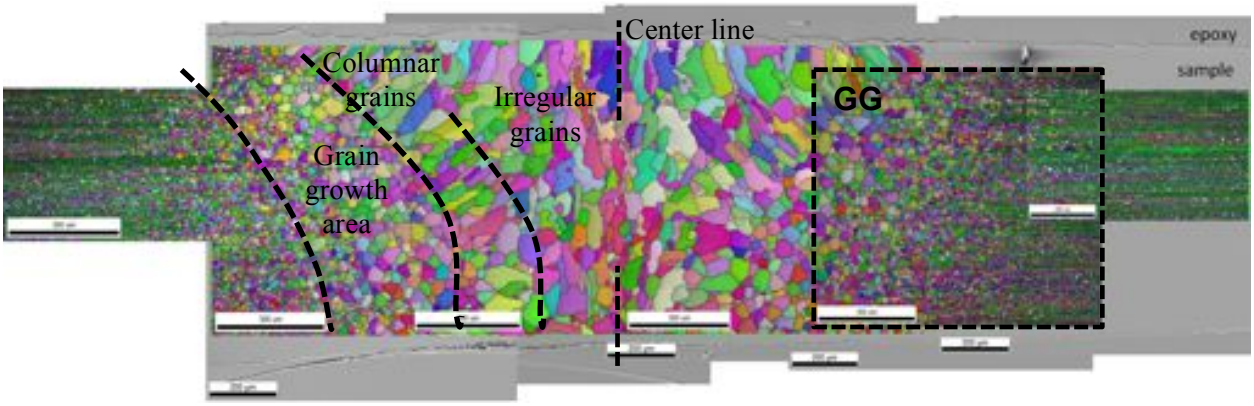

Figure 14: Stitched IPF maps (colored in the [010]-direction) showing the weldment and surrounding area for the C35M alloy. "GG" designates grain growth area; the texture for the GG-area shown in Figure 16.

The following area (heat-affected zone or grain growth area), as believed, did not experience melting but was subjected to high temperatures, well above the recrystallization temperature of the given material. In the grain growth area, one can see round shaped grains, which size decreased with the distance increasing from the weld centerline. The width of the grain growth area was about ~400 μm and this value varied with the specimen thickness. It is difficult to define the exact boundary of the grain growth area since the transition to the parent material was quite smooth. The grain growth area followed an area that experienced partial recrystallization and after that by parent material.

Figure 15 demonstrate the central portion of Figure 14 with the weld centerline, columnar grain area, and grain growth area visible. It should be noted that one of the present project goals was to evaluate the weldability of the advanced alloys. As follows from Figure 15, the weldment contained no crack, pores or rough inclusions confirming the acceptable weldability of the studied material.

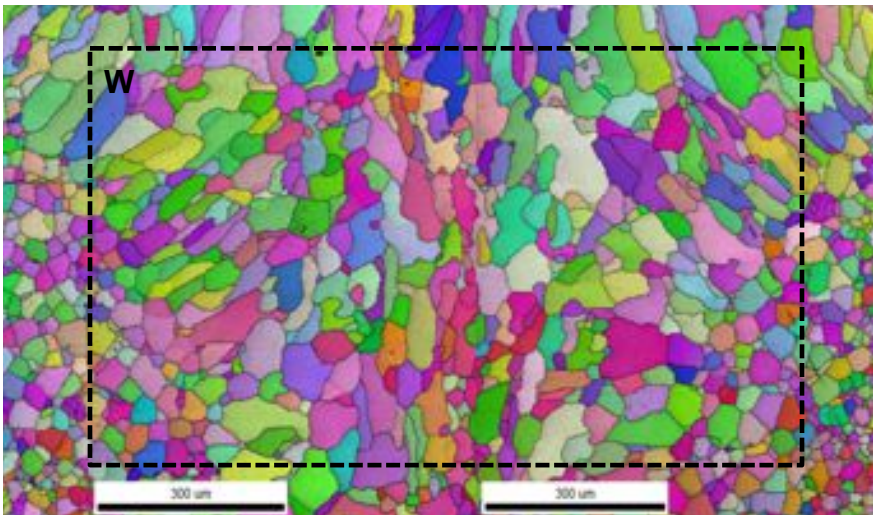

Figure 15: The enlarged view of the center area of the weldment shown in Figure 14. "W" and dashed rectangle depicts the area used in the texture calculation (Figure 16).

Figure 16 demonstrates the texture evolution as a function of distance from the weldment center. The most remote area (at the distance, d, of 3.9 mm from the weld centerline) demonstrated strong texturing (up to 5.6× random); grains oriented close to [010] regarding the rolling direction dominate the structure which is close to the texturing seen in the parent material, Section 6.2.1.1.1. The structure experienced light changes at the distances of ~2.7 and ~1.5 mm with some weak decrease in the fraction of grains oriented close to [010]. At the distance of ~1 mm, strong recrystallization and grain growth occurred; the intensity of the [010]-texture decreased down to ~2×random. Interestingly, many newly appeared grains had the orientation close to [112]; the intensity of this orientation component increased compared to the parent material. It appears that the grain orientation in the weldment, which experienced melting, (Figure 16) is not fully random; however the texturing is relatively weak, ~2×random.

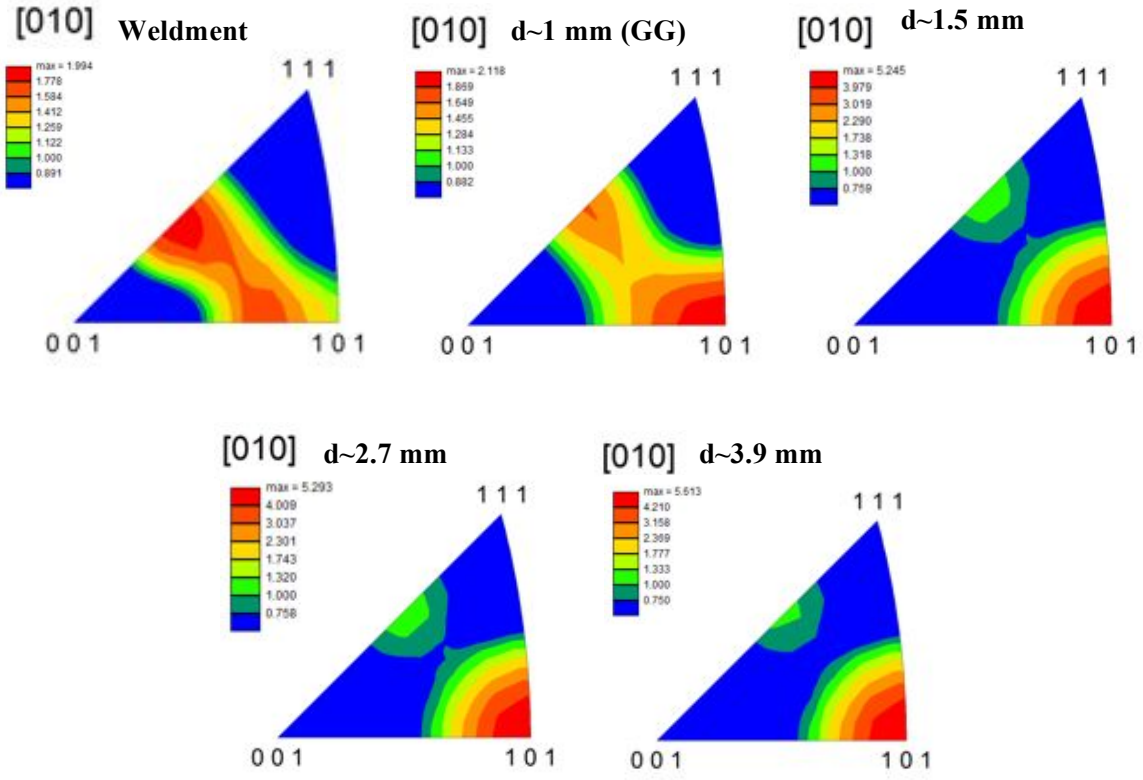

Figure 16: Texture in the C35M alloy at different distances from the weldment center. "Weldment" location corresponds to the central area designated as W in Figure 15. 1-mm distance corresponds to the grain growth (GG) area in Figure 14. Distances are quoted in reference to the weld centerline.

The transition between grain growth area and parent material is of interest from an EBSD point of view. Recrystallization and grain growth propagated in the parent material in a non-uniform way, Figure 17. The growing grains appeared along some preferable lines and propagated into the parent material leaving elongated "islands" of parent material behind. It may be clearly seen in EBSD IQ (image quality) maps, Figure 17. The IQ parameter is sensitive to the local defect (dislocation) density and increases during recrystallization. The change in the color separates parent (dark-gray, non-recrystallized) and recrystallized material (light-gray).

All analyzed areas (e.g., weldment, grain growth area, heat-affected zone) were defect free and demonstrated no cracking nor any other welding-induced defect.

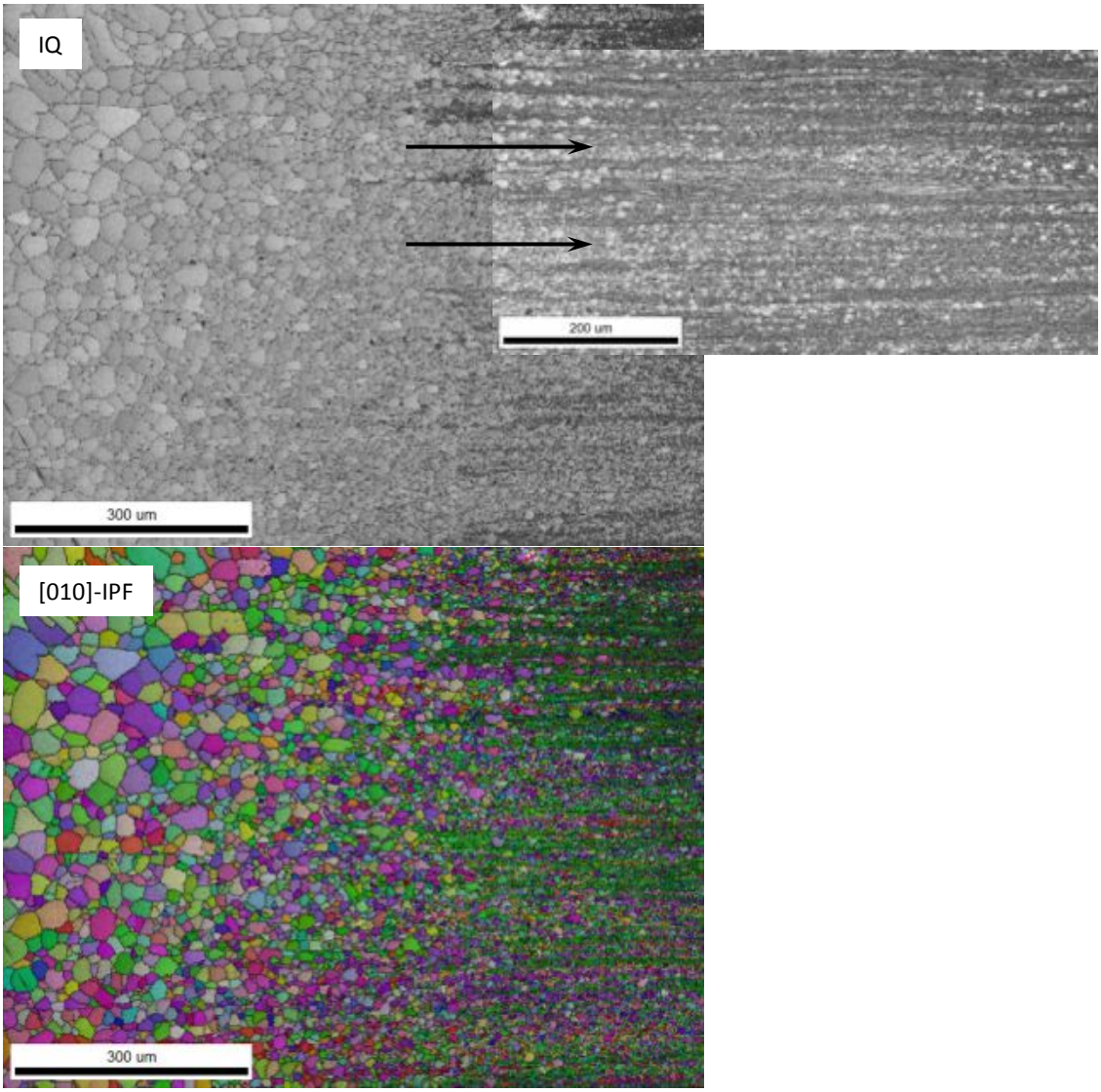

Figure 17: Transition from the grain growth area to the parent material for the C35M alloy.

6.2.1.2.2 C37M alloy

The weldment of the C37M alloy (Figure 18) contained the same specific zones as C35M: irregular gains at the center, area with columnar grains, grain-growth area, etc. No pronounced difference was observed.

Interestingly, the analyzed specimen contained a manufacturing defect (a crack formed along the rolling direction). The defect was fully cured by welding (Figure 18, Figure 19): it was still present in the grain growth area, which did not experience melting but disappeared in the fusion zone. Weak signs stringers were also observed in the right part of Figure 18, and this defect also disappeared in the weldment.

The texture evolution in the C37M alloy was also similar to the C35M alloy. The parent texture (3×random at [101]) became weak and disappeared in the weldment, Figure 20. The resulting texture was relatively weak, with only 2.3×random.

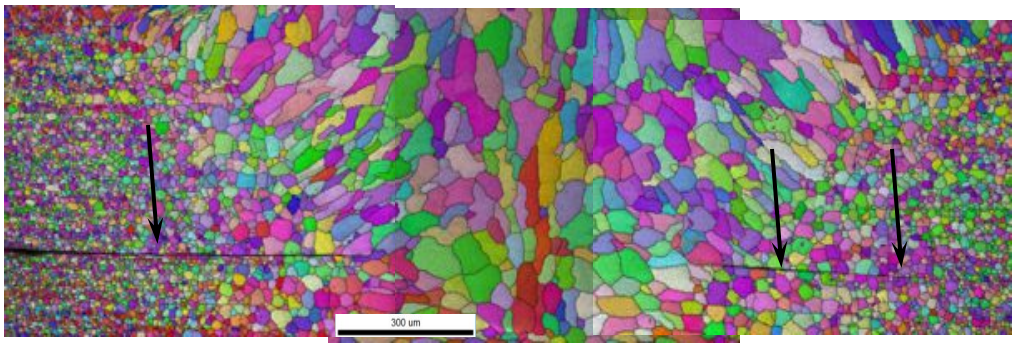

Figure 18: The central area of the C37M alloy weldment. Black arrows points to the defects in the parent plate.

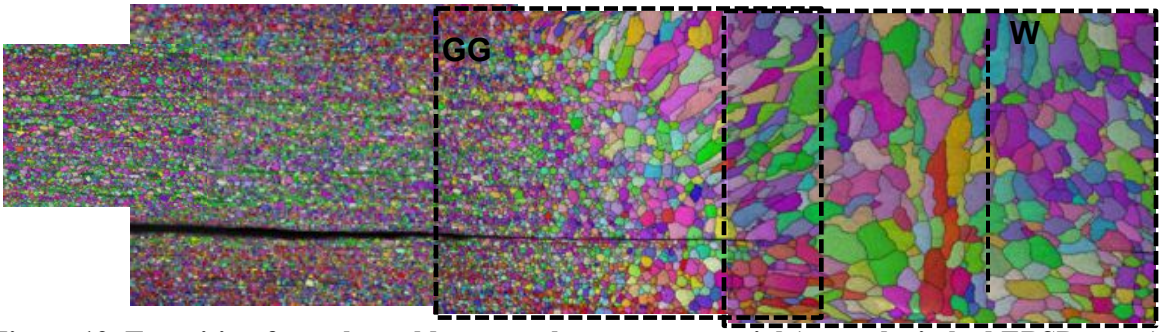

Figure 19. Transition from the weldment to the parent material (several stitched EBSD scans). Dash line indicates the weldment center.

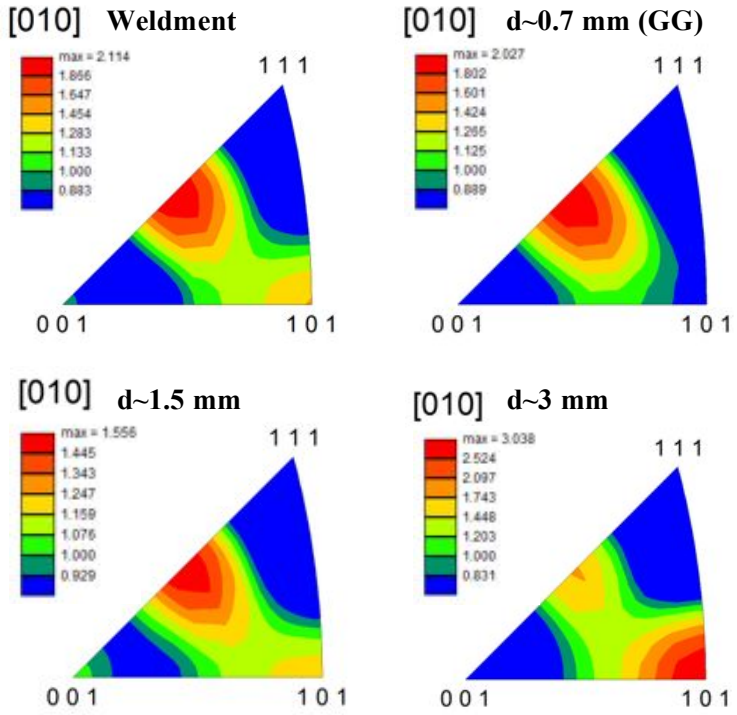

Figure 20: Texture evolution in the C37M alloy during welding. "Weldment" corresponds to the central area designated as W in Figure 19. 1-mm distance corresponds to the grain growth (GG) area in Figure 19. Distances are quoted in reference to the weld centerline.

6.2.1.2.3 C35M01T alloy

The addition of nominally 0.1% TiC did not change the visible grain morphology in the weldment, Figure 21. The grain size and shape were close enough to the parent C35M alloy. The only noticeable change was the increase in the fraction of "curved" boundaries with specific zig-zag behavior. Such boundaries were much rarer in the parent alloy. Additionally, numerous small black dots were observed in the IQ maps in this alloy but not in C35M. These dots are believed to be rough carbide particles. No welding defects were observed suggesting acceptable weldability of the material with 0.1% TiC.

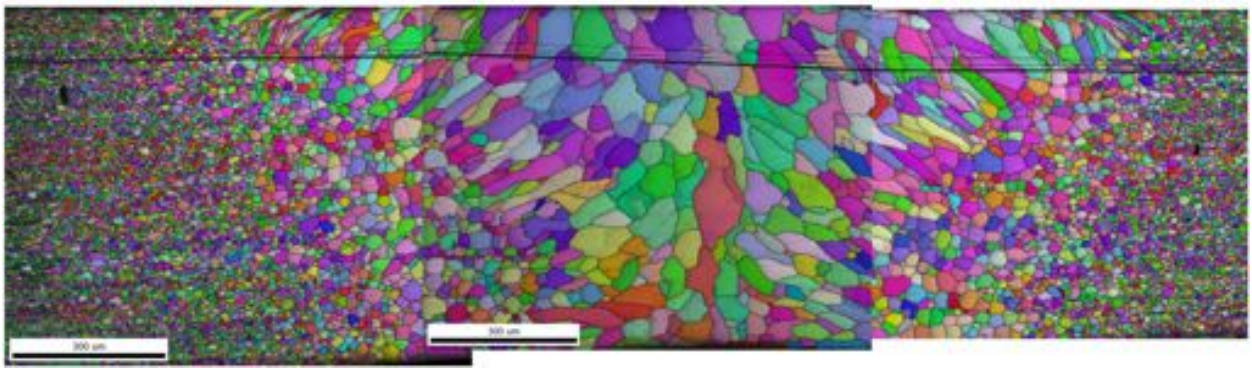

Figure 21: The central area of the C35M01TC alloy weldment. One can see a few rough scratches across the stitched image.

6.2.1.2.4 C35M03TC alloy

The further increase in the TiC content (to nominally 0.3%) did not lead to significant grain morphology change, Figure 22. As before, grain size and shape were similar to the parent C35M alloy. However, curved grain boundaries became more common. No welding defects were observed suggesting good weldability of the material with nominally 0.3% TiC.

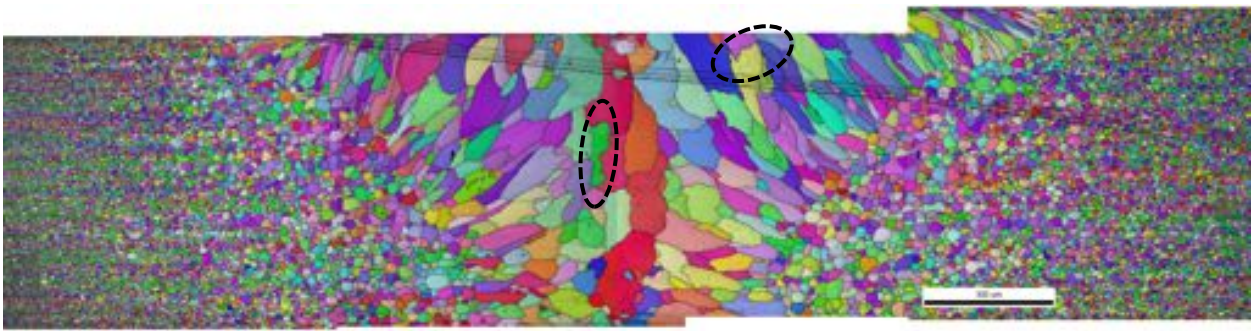

Figure 22: Weldment structure in the C35M03TC alloy. Black dashed ovals show some areas with curved grain boundaries. Few rough scratches are also visible.

6.2.1.2.5 C35M10TC alloy

The increase of TiC content from nominally 0.3 to 1% had a strong impact on the weldment structure and grain morphology, Figure 23. The grain size of the weldment center decreased up to 3-5 times. Columnar grains became smaller and more elongated. Grain boundary morphology also changes with curved (or torturous) boundaries dominating the weldment. At the same time, no welding defects like cracks, lack of fusion, or pores were observed. Thus, the nominal 1% TiC addition had a positive impact on grain refinement and also kept the acceptable weldability supporting our expectation and the goals of the present project.

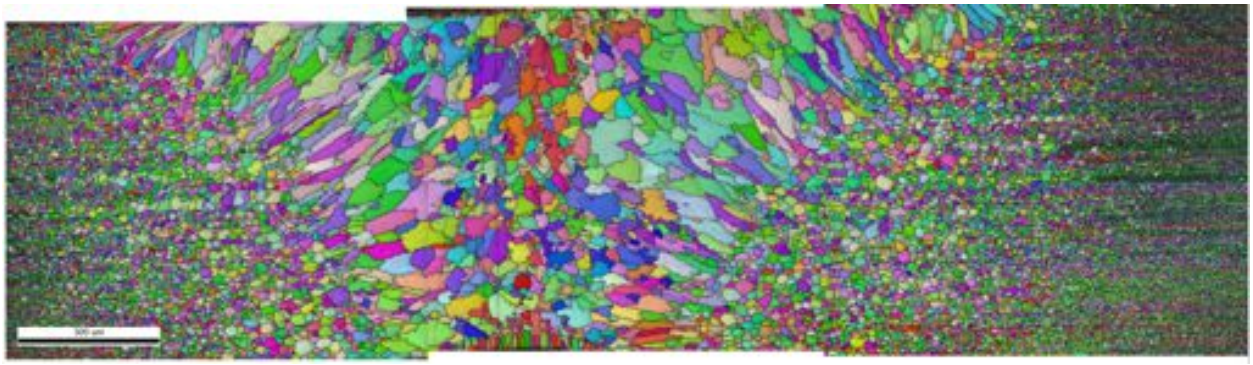

Figure 23: Weldment structure in the C35M10TC alloy. One can see smaller grain size in the weldment compared to other alloys.

6.3 The role of TiC-addition on grain morphology and growth during welding

Figure 24 summarizes the role of the TiC-addition on the weldment structure. Grain morphology did not change in C35M01TC alloy compared to the parent material. The only difference was few curved grain boundaries. C35M03TC alloy weldment contained comparable grains and larger fraction of the curved grain boundaries. C35M10TC alloy weldment had much smaller grain size (3-5 times smaller), and most of the grain boundaries had complex, curves shape.

The increasing addition of TiC dispersions in the base FeCrAl matrix during autogenous, bead-on-plate welding appears to increase the fraction of grain boundaries pinned during the melt and solidification process. The resulted grain growth is stunted. This results in the decreasing grain size and the increasing "wavy" or "tortuous" grain boundary appearances with increasing TiC additions in Figure 24. The elongated grains for all alloys indicate this mechanism is strongly inherent in the fusion zone only, the regions where melting did not occur does not seem to have the same mechanisms for stunting grain growth. It is also unclear if the observed microstructural differences between the alloys with TiC additions will be observed using different welding techniques, such as GTAW or electron-beam welding, or even with varying LBW parameters as all three alloys were welded using the same conditions in this study. Further work is needed to conclusively determine the effect of TiC additions on the weldability and the applicability of using such mechanisms to increase the weldability of FeCrAl alloys.

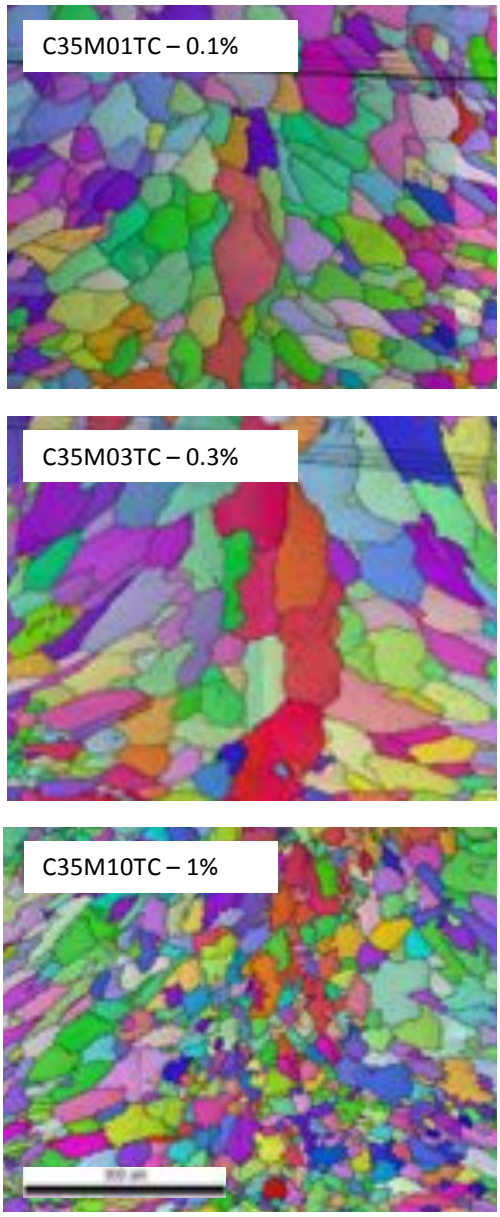

Figure 24: Comparison of the grain shape in the central area of the weldments for alloys with TiC-addition. Magnification and scale bar are the same for all images.

6.4 On-going and future work

The results presented above exclude analysis on the welded C36M and welded C35MN alloys. On-going work is currently being completed to execute SEM-EBSD analysis of weldments made from these alloys as well and will be compared to the results presented here. Also, microhardness mapping across the same areas of interest for SEM-EBSD is currently on-going. For example, Figure 25 shows a hardness map using a 300 g load, a 10 s dwell time, and 100 µm spacing on the C35M specimen shown in Figure 14. These maps can reveal confluences between microstructure and mechanical properties. Figure 25 shows the drop in hardness ~1 mm from the weld centerline which correlates with the fusion zone, columnar grain region, and grain growth regions depicted in Figure 14. Hardness mapping will be completed on all welded samples to determine the influence of the change in microstructures observed previously, with

changes in mechanical properties. Finally, SS-J3 and SS-2E tensile test specimens will be tested using digital image correlation (DIC) to determine the deformation mechanics of the weldments during uniaxial tensile testing.

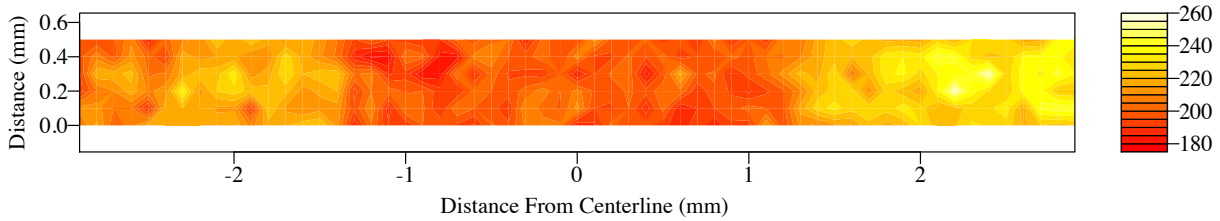

Figure 25: Microhardness (Hv 0.3) map in the cross-section of a LBW weldment in C35M alloy. Map shows a loss in the hardness within the regions of the fusion zone, columnar grains, and grain growth areas shown in Figure 14.

7. CONCLUSIONS

The results discussed in the present report provide the foundational understanding on the alloy development efforts towards FeCrAl alloy(s) specifically designed to have enhanced weldability and radiation tolerance for nuclear power production applications. It was found that optimization of both the microstructure and the alloy chemistry is needed to meet or exceed benchmarks for performance. For example, Cr, Al, and minor alloying elements such as Mo and Si were found to influence the phase stability of the alloys in the temperature range of 400-475°C. Higher Al contents suppressed the hardening and hence the formation of the deleterious Cr-rich α' while Mo and Si seemed to intensify the hardening response. Cr was also found to increase the hardening in the alloys. These results suggest chemistry control is a key factor in suppressing the precipitation of the Cr-rich α' which is important for reducing the hardening and embrittlement of these alloys while in-reactor.

Chemistry was found to be less significant for hydrogen uptake in the investigated advanced FeCrAl alloys. Due to the low solubility and need for high hydrogen pressures, gaseous charging cannot be used to assess the hydrogen embrittlement of these alloys. Cathodic charging can, and it was found that varying the bulk Al content while maintaining a constant Cr content did not change the amount of hydrogen introduced into the alloys using the sample charging conditions. This result suggests the possibility for similar hydrogen embrittlement during welding regardless of the Al content when the Cr content is restricted to 13 wt.% Cr.

Welding using fusion based techniques resulted in significant changes in the microstructure of the FeCrAl alloys with pronounced changes in grain size and morphology over the base alloy and changes in local texturing of the alloy. This effect was found to be lessened in the C35M10TC alloy and further investigations are underway to determine the mechanical response of the weldments.

The results presented here indicate the advantages of optimizing both the microstructure and chemistry of FeCrAl alloys to obtain necessary properties and performance for nuclear power production including weldability, thermal stability, and radiation tolerance. The present study has stimulated more development into advanced FeCrAl alloys and new efforts will focus on the continued understanding between the confluence of chemistry and structure on performance to develop a nuclear grade FeCrAl alloy with enhanced weldability and radiation tolerance.

8. REFERENCES

[1] B.A. Pint, K.A. Terrani, M.P. Brady, T. Cheng, J.R. Keiser, High temperature oxidation of fuel cladding candidate materials in steam–hydrogen environments, Journal of Nuclear Materials, 440 (2013) 420–427.

[2] B.A. Pint, K.A. Unocic, K.A. Terrani, The effect of steam on the high temperature oxidation behavior of alumina-forming alloys, Materials at High Temperature, 32 (2014) 28-35.

[3] K.G. Field, X. Hu, K.C. Littrell, Y. Yamamoto, L.L. Snead, Radiation tolerance of neutron-irradiated model Fe–Cr–Al alloys, Journal of Nuclear Materials, 465 (2015) 746-755.

[4] R.B. Rebak, Alloy Selection for Accident Tolerant Fuel Cladding in Commercial Light Water Reactors, Metallurgical and Materials Transactions E, (2015).

[5] Y. Yamamoto, B.A. Pint, K.A. Terrani, K.G. Field, L.L. Snead, Development and property evaluation of nuclear grade wrought FeCrAl fuel cladding for light water reactors, Accepted in - Journal of Nuclear Materials, (2015).

[6] J. Tusek, A. Kosmac, U. Nartnik, A. Dejan, Welding of heat-resistant 20 % Cr - 5% Al steels, Z. Metallkd., 93 (2002) 310–314.

[7] H. El Kadiri, Y. Bienvenu, K. Solanki, M.F. Horstemeyer, P.T. Wang, Creep and tensile behaviors of Fe–Cr–Al foils and laser microwelds at high temperature, Materials Science and Engineering: A, 421 (2006) 168-181.

[8] J.N. Dupont, J.R. Regina, K. Adams, Improving the weldability of fecral weld overlay coatings, in: Fossil Energy Materials Conference, ORNL, Oak Ridge National Laboratory, 2007, pp. 131–137.

[9] J.R. Regina, J.N. Dupont, A.R. Marder, The effect of chromium on the weldability and microstructure of Fe-Cr-Al weld cladding, Welding Journal, 86 (2007) 170–178.

[10] K.G. Field, M.N. Gussev, Y. Yamamoto, L.L. Snead, Deformation behavior of laser welds in high temperature oxidation resistant Fe–Cr–Al alloys for fuel cladding applications, Journal of Nuclear Materials, 454 (2014) 352–358.

[11] S. Kobayashi, T. Takasugi, Mapping of 475°C embrittlement in ferritic Fe–Cr–Al alloys, Scripta Materialia, 63 (2010) 1104–1107.

[12] G. Bonny, D. Terentyev, L. Malerba, On the α–α′ miscibility gap of Fe–Cr alloys, Scripta Materialia, 59 (2008) 1193–1196.

[13] K.G. Field, S.A. Briggs, P.D. Edmondson, X. Hu, K.C. Littrell, R.H. Howard, C.M. Parish, Y. Yamamoto, Evaluation of the Effect of Composition on Radiation Hardening and Embrittlement in Model FeCrAl Alloys, Oak Ridge, TN, ORNL/TM-2015/518, 2015.

[14] S.J. Zinkle, A. Möslang, T. Muroga, H. Tanigawa, Multimodal options for materials research to advance the basis for fusion energy in the ITER era, Nuclear Fusion, 53 (2013) 104024.

[15] W. Li, S. Lu, Q.-M. Hu, H. Mao, B. Johansson, L. Vitos, The effect of Al on the 475°C embrittlement of Fe–Cr alloys, Computational Materials Science, 74 (2013) 101–106.

[16] K.G. Field, M.N. Gussev, Y. Yamamoto, X. Hu, R.H. Howard, Preliminary Studies on the Fabrication and Characterization of Fe-Cr-Al Alloys Designed to Have Enhanced Weldability and Radiation Tolerance, Oak Ridge, TN, ORNL/TM-2015/192, 2015.

[17] K.G. Field, R.H. Howard, Y. Yamamoto, Design of Experiment for Irradiation of Welded Candidate Fe-Cr-Al Alloys Oak Ridge, TN, ORNL/TM-2015/375, 2015.

[18] P.J. Grobner, The 885F (475C) embrittlement of ferritic stainless steels, Metallurgical Transactions, 4 (1973) 251–260.

[19] J.J. Heger, 885F embrittlement of the ferritic chromium-iron alloys, Metal Progress, (1951) 55–61.

[20] C. Capdevila, M.K. Miller, G. Pimentel, J. Chao, Influence of recrystallization on phase separation kinetics of oxide dispersion strengthened Fe–Cr–Al alloy, Scripta Materialia, 66 (2012) 254–257.

[21] M. Courtnall, F. Pickering, The effect of alloying on 485 C embrittlement, Metal Science, 10 (1976) 273-276.

[22] F. Bergner, C. Pareige, M. Hernández-Mayoral, L. Malerba, C. Heintze, Application of a three-feature dispersed-barrier hardening model to neutron-irradiated Fe–Cr model alloys, Journal of Nuclear Materials, 448 (2014) 96–102.

[23] X. Hu, K.A. Terrani, B.D. Wirth, Hydrogen desorption kinetics from zirconium hydride and zirconium metal in vacuum, Journal of Nuclear Materials, 448 (2014) 87-95.

[24] Y. Kim, Y. Kim, D. Kim, S. Kim, W. Nam, H. Choe, Effects of Hydrogen Diffusion on the Mechanical Properties of Austenite 316L Steel at Ambient Temperature, Materials Transactions, 52 (2011) 507-513.

[25] M. Hoelzel, S.A. Danilkin, H. Ehrenberg, D.M. Toebbens, T.J. Udovic, H. Fuess, H. Wipf, Effects of high-pressure hydrogen charging on the structure of austenitic stainless steels, Materials Science and Engineering: A, 384 (2004) 255-261.